Published in final edited form as:
Circ Cardiovasc Imaging. 2011 July ; 4(4): 415–424. doi:10.1161/CIRCIMAGING.111.963868.

X-Ray Magnetic Resonance Fusion to Internal Markers and Utility in Congenital Heart Disease Catheterization

Yoav Dori, MD, PhD, **Marily Sarmiento, MSEE, MBA**, **Andrew C. Glatz, MD**, **Matthew J. Gillespie, MD**, **Virginia M. Jones, RN, BSN**, **Matthew A. Harris, MD**, **Kevin K. Whitehead, MD, PhD**, **Mark A. Fogel, MD**, and **Jonathan J. Rome, MD**
Department of Cardiology, The Children's Hospital of Philadelphia, Philadelphia, PA (Y.D., A.C.G., M.J.G., V.M.J., M.A.H., K.K.W., M.A.F., J.J.R.); and Siemens Healthcare, Malvern, PA (M.S.)

Abstract

Background—X-ray magnetic resonance fusion (XMRF) allows for use of 3D data during cardiac catheterization. However, to date, technical requirements have limited the use of this modality in clinical practice. We report on a new internal-marker XMRF method that we have developed and describe how we used XMRF during cardiac catheterization in congenital heart disease.

Methods and Results—XMRF was performed in a phantom and in 23 patients presenting for cardiac catheterization who also needed cardiac MRI for clinical reasons. The registration process was performed in <5 minutes per patient, with minimal radiation (0.004 to 0.024 mSv) and without contrast. Registration error was calculated in a phantom and in 8 patients using the maximum distance between angiographic and 3D model boundaries. In the phantom, the measured error in the anteroposterior projection had a mean of 1.15 mm (standard deviation, 0.73). The measured error in patients had a median of 2.15 mm (interquartile range, 1.65 to 2.56 mm). Internal markers included bones, airway, image artifact, calcifications, and the heart and vessel borders. The MRI data were used for road mapping in 17 of 23 (74%) cases and camera angle selection in 11 of 23 (48%) cases.

Conclusions—Internal marker–based registration can be performed quickly, with minimal radiation, without the need for contrast, and with clinically acceptable accuracy using commercially available software. We have also demonstrated several potential uses for XMRF in routine clinical practice. This modality has the potential to reduce radiation exposure and improve catheterization outcomes.

Keywords

x-ray magnetic resonance fusion; MRI; registration; catheterization

Traditional fluoroscopically guided cardiac catheterization is sufficient to guide catheterization procedures, with good results. However, fluoroscopy requires the use of ionizing radiation, has poor soft tissue definition, and only provides 2D projections of

Correspondence to Yoav Dori, MD, PhD, 34th St and Civic Center Blvd, Philadelphia, PA 19104. doriy@email.chop.edu.

Disclosures
None.

The online-only Data Supplement is available at http://circimaging.ahajournals.org/cgi/content/full/CIRCIMAGING.111.963868/DC1.

complex 3D anatomy. As interventional procedures have become more complex, it is becoming apparent that in many instances this imaging modality is suboptimal. One option is to use real-time MRI to guide interventions.[1] Although this strategy has promise, the lack of MRI-compatible wires and catheters and difficulties with catheter tracking limit the current use of this modality.

An alternative to exclusive real-time MRI-guided interventions or fluoroscopy-only guided interventions is to use an approach in which 3D data sets from either computed tomography (CT), rotational angiography, or MRI are fused to the x-ray images to provide additional information while still taking advantage of the good spatial and temporal resolution offered by conventional fluoroscopy. Fusion of CT and rotational angiography images has been reported in electrophysiological studies.[2-7] Registration of CT and rotational angiography to x-ray images is simpler because of the similarity of the imaging methods, making them amenable to automated intensity–based registration approaches.[8,9] Registration of MRI images is more complex because of the inherit difference in the imaging modalities. To overcome this problem, fusion of MRI images is often carried out with external fiducial markers. Several groups have reported fiducial marker–based registration in cardiac and vascular interventions.[10-13] One group has reported on a registration method that did not require fiducial markers but used a catheter-based calibration scheme and visual matching to register MRI data for electroanatomic mapping, with an accuracy on the order of 2 mm.[14] Accurate registration of MRI data to rotation angiography volumes has also been reported in neurological interventions.[15]

In the present study, we report on an internal-marker XMRF method that we have developed that does not require contrast or external fiducial markers, requires only minimal radiation exposure, and can be done with commercially available software, making it feasible to now perform XMRF on a routine clinical basis. We then describe some of the uses we found for this modality during cardiac catheterization in congenital heart disease.

Methods

Patient Selection

XMRF was performed on patients presenting to our catheterization laboratory between March 1, 2010, and August 1, 2010, who also needed cardiac MRI for clinical reasons or who had undergone MRI examination in the past year. In the present study, we did not target a specific patient population and only excluded patients who had contraindicating findings on MRI, such as significant artifact from metallic devices.

Magnetic Resonance Imaging

MRI scans were performed on a Magnetom Avanto 1.5-T Siemens scanner. All patients underwent cardiac MRI consisting of (1) balanced steady-state free precession (bright blood) transverse stack, which extended from the thoracic inlet to the superior portion of the liver, (2) half-Fourier single-shot turbo spin-echo (dark blood) transverse stack spanning the same region, (3) balanced steady-state free precession cine imaging including a 2-chamber view, 4 chamber view, and short-axis stack for anatomy and to quantify ventricular function, (4) velocity-encoded cine imaging of the ascending aorta, vena cava, pulmonary arteries, and in some cases, pulmonary veins for flow quantification, and (5) Angiography High Spatial and Temporal Resolution MRA (syngo TWIST) of the heart and great vessels for anatomy. Typical imaging parameters are listed in Table 1. The images were then electronically transmitted to the work station in the fluoroscopy suite for review and rendering. The sequences that were selected for registration were volume-rendered and cropped using the syngo InSpace work station. For phantom experiments, MRI scanning consisted of a

balanced steady-state free precession (bright blood) transverse stack of the phantom and Angiography High Spatial and Temporal Resolution MRA imaging of the phantom without contrast injection.

XMRF Protocol

XMRF procedures were performed using a Siemens Axiom Artis cardiac x-ray system connected by a Miyabi sliding table to the MRI scanner (Siemens, Erlangen, Germany). In cases in which MRI and catheterization were performed sequentially, the patients were positioned on the Miyabi sliding table before the MRI procedure by the cath lab staff. Patients who were small (usually age <4 years) received general endotracheal anesthesia and were positioned on the Miyabi table with arms elevated during both procedures. Larger patients received conscious sedation and were positioned with the arms down during the MRI scan. The arms were elevated after transfer to the cath lab before the registration process. Patients were transferred to the x-ray room after completing the MRI study by means of the sliding table. In those cases, in which the 2 studies were done separately, the patients were positioned on the MRI and x-ray table in the normal fashion, ensuring that the patients were supine and aligned along the long axis of the table during both procedures. The patients were then moved to isocenter, and a rotational angiography spin was performed without using radiation (blank spin). This produces a parameter file containing the bed and gantry coordinates and the dimensions of a theoretical x-ray space derived from geometric considerations. This file was then used for the first step of the registration process.

Registration

The image registration protocol is shown in Figure 1. Image registration was carried out with the commercially available Siemens “syngo InSpace 3D/3D fusion,” “iPilot dynamic,” and “register to patient” functionalities (Siemens, Erlangen, Germany). The “syngo InSpace 3D/3D fusion” functionality was used for the first portion of the registration process, which is divided into 2 steps. First, the software uses an automatic linear transformation algorithm to translate the MRI coordinate system into the x-ray space and to scale the MRI data set. This step, which is essential for completion of the fusion process, does not use any of the rotational angiography pixel information but is based solely on geometric considerations derived from the gantry and table position when the patient’s region of interest is in isocenter. Normally, 3D rotational angiography pixel information is present from a radiocontrast spin, allowing for the second step, which involves either automatic intensity–based registration or visual matching manual registration of the 3D angiography pixel data to the 3D MRI data. However, in the method we have developed, because the rotational angiography spins were acquired with blocked radiation that do not contain any pixel information, the second 3D/3D registration step was bypassed. Consequently, an additional step was needed to accurately register the MRI data. This was achieved using the “register to patient” and “iPilot dynamic” functionalities, which have algorithms to automatically register the live 2D fluoroscopy image to the 3D data set in any camera angle and also allows for visualization and fading between the live 2D and 3D data sets as well as having functionalities for 2D/3D visual matching manual registration. In the current software version, only the anteroposterior (AP) camera is registered. The manual registration step involves translation along the 3 spatial coordinates of the internal marker of choice as seen on the MRI image to match the internal marker as seen on the x-ray image. Two orthogonal maximal field-of-view fluoroscopy images, one in the AP projection (0°) and the second with the AP camera in the lateral projection (90°), were used for this purpose. On completion of the registration process, the fused 3D MRI and live fluoroscopy images were displayed during the catheterization using “iPilot dynamic,” which was also used to correct for misregistration caused by patient motion.

Patients were meticulously positioned before both procedures so that rotation of the MRI volume was not needed. Once the registration process was completed, all sequences from the MRI scan were registered and all the sequences were registered to the camera and to the table so that rotation of the camera or movement of the table produced an equivalent movement in the registered MRI volume (Figure 1, bottom).

The accuracy of manual visual matching image registration to cardiac borders has already been established in a phantom and in patients.[14] In the current study, we tested the registration accuracy using a phantom 18×15×6 cm containing 2 layers of dual-modality fiducial markers (Beekley Corporation, Bristol, CT) suspended in water using a polymer scaffold (Figure 2A and 2B). The phantom contained 9 markers. After performing registration to the central marker, the registration error was calculated as the distance between the center of the each of the remaining 8 markers, as seen on the x-ray image, and the same marker as seen on the overlaid MRI image in the AP, right axial oblique (RAO), and left axial oblique (LAO) projections (Figure 2C through 2E). Marker boundaries and coordinates of the marker geometric centers were determined using the ImageJ open source image analysis package (US National Institutes of Health, Bethesda, MD). The distance between the 2 centers was calculated using $d=\sqrt{\left([C_{1x}-C_{2x}]^2+\left[C_{1y}-C_{2y}\right]^2\right)}$, where d is the calculated distance, C_{1x} and C_{1y} are the x and y coordinates of the center of the marker as seen on the x-ray image, and C_{2x} and C_{2y} are the x and y coordinated of the center of the same marker as seen on the overlaid MRI image. In patients, the error was calculated in 8 patients who had angiography of the proximal right pulmonary artery segment located between the main pulmonary artery and the right upper pulmonary artery (RUPA) branch, with the camera in the AP projection and whose studies were done sequentially. The registration error (ε) was assessed by 2 observers (a cardiologist familiar with the underlying anatomy and a researcher) by measuring the maximal distance between angiographic vessel borders and 3D model boundaries during contrast injection (Figure 2F).

Registration was performed to internal markers including the heart and vessel borders, bones, conduit calcification, imaging artifact, and airway. Registration to bone was performed with a T1-weighted short stack (3 to 5 slices; TR, 2000; TE, 45; inversion time, 900 msec; slice thickness, 3 mm; bandwidth, 500; matrix, 256×256; flip angle, 150; field of view, 200×200) of either the sternum and anterior aspect of the rib cage or the spine and posterior rib cage (Figure 3A through 3H). Registration to the airway was done with a dark-blood short stack (3 to 4 slices, 3 mm per slice) centered on the carina (Figure 3I through 3L). Artifacts included susceptibility artifact from sternal wires and stents (Figure 4A through 4D). Registration was also performed to a ring of calcification in the distal end of a right ventricle to pulmonary artery (RV-PA) conduit (Figure 4E through 4F). Registration to the heart and vessel borders was performed with either volume-rendered MRI images or maximal intensity projection–rendered MRI images showing the largest cross section of the heart and great vessels in the AP projection (Figure 5).

Statistical Methods

Summary data are presented as frequency with percentage of total for count data, median with range for non-normally distributed continuous variables, and mean with standard deviation for normally distributed continuous variables.

This study was conducted with approval from our institutional review board (IRB No. 10-007587).

Results

To date, we have performed 23 XMRF procedures in our cardiac catheterization laboratory. Patient characteristics are summarized in Table 2. MRI was performed on the same day as the catheterization in 19 of 23 (83%) of the patients. The longest time interval between the MRI and the catheterization was 12 months. XMRF was used across a wide range of patient ages and sizes. Registration was performed to the heart and vessels in 16 of 23 (69%) of the patients, to bones in 2 of 23 (9%) patients, to the airway in 2 of 23 (9%) patients, to artifact in 2 of 23 (9%) patients, and to conduit calcification in 1 of 23 (4%) patients.

The entire registration process was performed in <5 minutes per patient and with minimal radiation (0.004 to 0.024 mSv). The radiation was calculated on the basis of a 1-second exposure at 15 frames/s, using the method described elsewhere.[16] We also calculated the total radiation exposure in 8 of 23 patients who had a purely diagnostic cardiac catheterization and had the total dose-area product recorded. For these patients, the calculated total dose-area product had a median of 2.65 mSv with a range of (1.84 to 6.42).

In the phantom experiments, the registration error with the camera in the AP projection had a mean of 1.15 mm (standard deviation, 0.73; n=8), with the camera in the RAO projection the mean error was 1.17 mm (standard deviation, 0.51; n=8), and in the LAO projection the mean error was 1.35 mm (standard deviation, 0.58; n=8). In patients, the measured registration error had a median of 2.15 mm (interquartile range, 1.65 to 2.56 mm).

XMRF was mainly used for roadmapping and for camera angle selection. In 17 of 23 cases the overlaid images were used for roadmapping during the procedure. Roadmaps for the entire catheterization procedure were created before the start of the catheterization and stored as a collection of bookmarks that were retrieved when the structure of interest was reached. An example of how XMRF was used for roadmapping is depicted in Figure 6. Whole volume-rendered images or images that were cut to delineate certain structures were used for this purpose (Figure 6A through 6C). Figure 6 shows the heart of a patient with a small RV-PA conduit and left pulmonary artery stenosis. A coronal cut-plane was created before the catheterization and used as a roadmap for navigation from the inferior vena cava to the conduit (Figure 6B and 6E). After entering the conduit, an oblique cut-plane showing the left pulmonary artery was loaded and used as a roadmap to enter the left pulmonary artery (Figure 6C and 6F). In 10 of 23 cases, it was thought that the anatomic structures of interest would not have easily been entered without the roadmap unless contrast injection was performed. In those cases in which devices were placed, the XMRF roadmaps were used for preliminary device positioning, although in all instances, final device positions were performed on the basis of contrast angiograms.

Camera angle selection on the basis of MRI data were performed in 11 of 23 cases (Table 3). The relevant anatomic information was obtained by viewing the 3D-reconstructed image from different angles and then choosing the camera angle that would best profile the structure of interest. The camera was then rotated to the desired position and the fused image was reviewed to ensure that there was nothing on the fluoroscopy image that could interfere with the angiogram and to confirm that the chosen angle produced the desired result. In the majority of these cases it was thought that the 3D anatomy would not have been obtained by a single contrast injection using conventional camera angles (Figure 7).

Although it was not a major focus of this work, we also used the nonfused 3D MRI anatomic data before the catheterization procedures to perform preliminary catheter and device selection and sizing on the basis of MRI measurements. An example demonstrating how the nonfused 3D MRI anatomic data were used is shown in Figure 8. Figure 8 depicts a case with stenosis in the proximal pulmonary arteries and the proximal RV-PA conduit.

After reviewing the MRI data, we determined that 3 stents would be needed, each with a different length and diameter.

Discussion

The syngo InSpace 3D/3D fusion functionality was designed to enable accurate registration of previously acquired MRI data to 3D syngo rotational angiography data sets. However, this requires a significant amount of radiation and contrast, making it impractical for routine use in children. We report on a method that we have developed to perform the registration process using the same commercially available software tools but with minimal radiation and without the need for contrast injection, making it feasible to perform XMRF on a routine clinical basis. Furthermore, we have shown that the registration in a phantom and in patients is accurate, with error values similar to those that have been previously reported.[14]

The current registration software requires that we perform a blank spin to acquire the table coordinates and the dimensions of the x-ray space. However, in practice this step could be easily eliminated because the registration parameters are derived exclusively from geometric consideration, such as the geometry of the gantry and the relative table position, which are fixed once the patient is placed in isocenter. Furthermore, the registration parameters for all possible camera angles can be derived from similar geometric considerations, which probably will increase the accuracy of the registration process in off-axis (steep) camera angles. At more extreme camera angles, other factors affecting the x-ray beam, such as x-ray beam distortion, also must be considered.

Rigid body registration algorithms result in an MRI volume whose shape is fixed in time. In reality, there are nonperiodic changes in the geometry of the heart and vessels caused by physiological factors, such as change in preload, and caused by distortion of the vessel conformation by stiff wires and catheters (Figure 8C). In addition, there are periodic changes from respiratory and cardiac motion that produce a time-varying registration error. The magnitude of the periodic errors in most cases does not exceed the error tolerance for most of the interventions that we encounter in congenital heart disease. In contrast, the nonperiodic errors, especially those caused by anatomy distortion by stiff wires and catheters, can be significant limiting the utility of this modality in certain situations. In these cases, nonrigid registration algorithms would need to be used.

Fiducial marker–based registration has been shown to be accurate to high spatial resolution under certain conditions, but this method has several drawbacks. First, it requires that the MRI scan immediately precede catheterization because the markers must remain attached during both procedures. Second, skin mobility and movement of internal organs relative to the skin can make this method inaccurate. Third, the need to include the markers in the MRI images requires a larger scanned volume, increasing imaging time, and could result in reduced imaging resolution. Fourth, fiducial markers can interfere with the catheterizer’s view and obstruct important structures during contrast angiograms. Last, fiducial marker–based registration requires propriety software that is not currently commercially available.

Internal marker–based registration offers several advantages over fiducial marker–based registration. Internal markers are inherently more stable. They allow for easy correction of patient motion and they do not interfere with contrast angiograms. Furthermore, internal marker–based registration alleviates the constraint imposed by fiducial marker–based registration, namely, the need to perform the MRI and the catheterization successively. In the present study, the heart and vessel borders were the most frequently used markers. In addition, we report on registration to other possible internal markers as a proof of concept and to show the generalizability of our methodology. In 2 cases, in which the heart and

vessel borders were not clearly visible because of significant pulmonary edema, registration was done to the airway. Registration to the imaging artifact, stent, and calcification were easy to implement and subjectively accurate, but although more common in pediatric patients, these markers are not routinely present. In addition, the flexibility of our methodology allows for switching between MRI volumes and markers quickly as well as for using multiple markers simultaneously.

MRI is able to provide diagnostic-quality 3D images in most cases, even in the presence of metallic artifact. In contrast to rotational angiography or CT, MRI does not require ionizing radiation and it provides hemodynamic data. Furthermore, the 3D anatomy of the entire circulatory system is obtained with a single contrast injection, allowing us to roadmap the entire procedure and select camera angles for all vessels before the start of the procedure. However, there are certain conditions, such as in the presence of epicardial pacemaker leads or stainless steel coils, in which MRI is either contraindicated or nondiagnostic. In these cases, other modalities such as CT or rotational angiography can be used if 3D data are needed.[16]

The ability to roadmap without the need for contrast offers a distinct advantage in certain cases because contrast is known to significantly affect hemodynamics. Furthermore, the ability to roadmap the entire procedure and store the roadmaps as bookmarks has the potential to save time and reduce radiation exposure and contrast load. However, there are 2 limitations to this roadmapping modality that must be considered. First, the spatial resolution of MRI is on the order of 1 mm, making contrast injections necessary for roadmapping in very small vessels. Second, as previously mentioned, the presence of stiff wires or catheters can significantly alter the geometry of the vessels, making roadmapping based on previously acquired images inaccurate.

In all cases in which the nonfused 3D MRI anatomic data were used for initial approximate sizing of devices, the actual final device sizing was obtained from measurements performed on contrast angiograms. Care must be taken in trying to size devices on the basis of MRI data. The diameter of vessels in volume-rendered data sets highly depends on thresholding levels and is consequently not reliable.[17] Sizing from noncontrast images, such as cine or bright-blood images, is potentially more accurate; however, one must take into account that the MRI images are averaged over multiple heart cycles and not obtained instantaneously, as is the case in angiography. In contrast to device diameter, sizing of device lengths can be more reliably determined from volume-rendered MRI data because this dimension is less dependent on rendering levels. Further studies must be conducted to determine if accurate sizing of devices based on MRI image can be reliably done.

The total dose-area product that we calculated in this study is lower than the results reported in the literature by Bacher et al[18] of 4.6 mSv (range, 0.6 to 23.2) for all types of congenital heart disease diagnostic procedures. However, certain limitations in the study make it impossible to say with certainty if these results are significant. First, in the present study, we only had a small number of patients with each type of disease, and, of those, only a small number had purely diagnostic procedures. Second, because we only studied patients who needed both a catheterization and MRI, there is a significant selection bias in the cases that we evaluated. Last, in the present study, there was a large variation in patient size and age. Further studies must be conducted to determine the true effect of the XMRF modality on radiation exposure.

In the present study, we describe the new XMRF method that we have developed and show how the XMRF modality can be used during cardiac catheterization. In addition, the substantial hemodynamic and 3D anatomic information obtained from the MRI scans could

allow us to plan the catheterization and may allow us to perform a more targeted catheterization aimed at only obtaining missing information. Further studies are currently underway to determine the effect of this modality on catheterization outcomes.

Limitations of the Current Study

In the current study, we describe the XMRF registration process and retrospectively discuss our early experience with this new modality in a relatively small number of patients and as such has several inherit limitations. Because of the way patients were selected, there may be significant selection bias. The clinical portion of the study is descriptive in nature; as such, we cannot draw definitive conclusions about the effect of this modality on catheterization outcomes. In particular, our assessments of the advantage that we derived from XMRF in specific cases were inherently subjective.

In patients, the registration error was calculated only in the AP projection during 1 phase of the cardiac cycle. Although we did perform angiograms in other angles and have subjectively seen accurate registration in off-axis angles, the small number of overlaid angiograms at each angle does not allow us to comment on the accuracy of the registration in all angles. However, it is likely that the registration error will increase with steeper camera angles. Also, we cannot comment on the dependence of the error on the temporal proximity of the MRI and catheterization studies because most of the MRI and catheterization cases were performed on the same day, and, although we demonstrated the feasibility of using internal markers other than the heart and vessel borders, the small number of cases that were performed using these markers make it impossible to comment on the accuracy of the registration to each of the different markers. In addition, in this work we did not account for periodic changes from respiratory and heart motion in the error calculation. In reality, these factors produce a time-varying error $\varepsilon(t)$ that must be calculated using more elaborate methods. Further studies must be conducted to determine how these different factors affect the registration process and utility.

Conclusions

XMRF to internal markers can be performed quickly, with clinically acceptable accuracy, without the need for contrast, and with minimal radiation exposure and using commercially available software tools, making it feasible to now perform XMRF on a routine clinical basis. XMRF was used for camera angle selection, preliminary device positioning, and for roadmapping. This modality has the potential to reduce radiation exposure and improve catheterization outcomes.

Supplementary Material

Refer to Web version on PubMed Central for supplementary material.

References

1. Saikus CE, Lederman RJ. Interventional cardiovascular magnetic resonance imaging: a new opportunity for image-guided interventions. J Am Coll Cardiol Cardiovasc Imaging. 2009; 2:1321–1331.
2. Knecht S, Skali H, O'Neill MD, Wright M, Matsuo S, Chaudhry GM, Haffajee CI, Nault I, Gijsbers GH, Sacher F, Laurent F, Montaudon M, Corneloup O, Hocini M, Haissaguerre M, Orlov MV, Jais P. Computed tomography-fluoroscopy overlay evaluation during catheter ablation of left atrial arrhythmia. Europace. 2008; 10:931–938. [PubMed: 18511437]

3. Sra J, Krum D, Malloy A, Vass M, Belanger B, Soubelet E, Vaillant R, Akhtar M. Registration of three-dimensional left atrial computed tomographic images with projection images obtained using fluoroscopy. Circulation. 2005; 112:3763–3768. [PubMed: 16344405]
4. Sra J, Narayan G, Krum D, Akhtar M. Registration of 3d computed tomographic images with interventional systems: implications for catheter ablation of atrial fibrillation. J Interv Card Electrophysiol. 2006; 16:141–148. [PubMed: 17139556]
5. Sra J, Narayan G, Krum D, Malloy A, Cooley R, Bhatia A, Dhala A, Blanck Z, Nangia V, Akhtar M. Computed tomography-fluoroscopy image integration-guided catheter ablation of atrial fibrillation. J Cardiovasc Electrophysiol. 2007; 18:409–414. [PubMed: 17284262]
6. Li JH, Haim M, Movassaghi B, Mendel JB, Chaudhry GM, Haffajee CI, Orlov MV. Segmentation and registration of three-dimensional rotational angiogram on live fluoroscopy to guide atrial fibrillation ablation: a new online imaging tool. Heart Rhythm. 2009; 6:231–237. [PubMed: 19187917]
7. Orlov MV. How to perform and interpret rotational angiography in the electrophysiology laboratory. Heart Rhythm. 2009; 6:1830–1836. [PubMed: 19959137]
8. Tomazevic D, Likar B, Pernus F. Three-D/2-D registration by integrating 2-D information in 3-D. IEEE Trans Med Imaging. 2006; 25:17–27. [PubMed: 16398411]
9. Tomazevic D, Likar B, Slivnik T, Pernus F. Three-D/2-D registration of CT and MR to x-ray images. IEEE Trans Med Imaging. 2003; 22:1407–1416. [PubMed: 14606674]
10. de Silva R, Gutierrez LF, Raval AN, McVeigh ER, Ozturk C, Lederman RJ. x-ray fused with magnetic resonance imaging (XFM) to target endomyocardial injections: validation in a swine model of myocardial infarction. Circulation. 2006; 114:2342–2350. [PubMed: 17101858]
11. Gutierrez LF, Ozturk C, McVeigh ER, Lederman RJ. A practical global distortion correction method for an image intensifier based x-ray fluoroscopy system. Med Phys. 2008; 35:997–1007. [PubMed: 18404935]
12. Gutierrez LF, Silva R, Ozturk C, Sonmez M, Stine AM, Raval AN, Raman VK, Sachdev V, Aviles RJ, Waclawiw MA, McVeigh ER, Lederman RJ. Technology preview: x-ray fused with magnetic resonance during invasive cardiovascular procedures. Catheter Cardiovasc Interv. 2007; 70:773–782. [PubMed: 18022851]
13. Rhode KS, Hill DL, Edwards PJ, Hipwell J, Rueckert D, Sanchez-Ortiz G, Hegde S, Rahunathan V, Razavi R. Registration and tracking to integrate x-ray and MR images in an XMR facility. IEEE Trans Med Imaging. 2003; 22:1369–1378. [PubMed: 14606671]
14. Ector J, De Buck S, Adams J, Dymarkowski S, Bogaert J, Maes F, Heidbuchel H. Cardiac three-dimensional magnetic resonance imaging and fluoroscopy merging: a new approach for electroanatomic mapping to assist catheter ablation. Circulation. 2005; 112:3769–3776. [PubMed: 16330683]
15. Levitt MR, Ghodke BV, Cooke DL, Hallam DK, Kim LJ, Sekhar LN. Endovascular procedures with CTA and MRA roadmapping. J Neuroimaging. Jul 23.2010 Epub ahead of print.
16. Glatz AC, Zhu X, Gillespie MJ, Hanna BD, Rome JJ. Use of angiographic CT imaging in the cardiac catheterization laboratory for congenital heart disease. J Am Coll Cardiol Cardiovasc Imaging. 2010; 3:1149–1157.
17. Valverde I, Parish V, Hussain T, Rosenthal E, Beerbaum P, Krasemann T. Planning of catheter interventions for pulmonary artery stenosis: improved measurement agreement with magnetic resonance angiography using identical angulations. Catheter Cardiovasc Interv. 2011; 77:400–408. [PubMed: 20549687]
18. Bacher K, Bogaert E, Lapere R, De Wolf D, Thierens H. Patient-specific dose and radiation risk estimation in pediatric cardiac catheterization. Circulation. 2005; 111:83–89. [PubMed: 15611374]

CLINICAL PERSPECTIVE

Fluoroscopy is the main imaging modality used to guide catheterization procedures. However, several limitations including poor soft tissue definition, the use of ionizing radiation, and lack of 3D data make this imaging modality suboptimal. In the x-ray magnetic resonance fusion (XMRF) modality, 3D MRI data are overlaid onto live fluoroscopic images during the catheterization procedure. This takes advantage of the high spatial and temporal resolution provided by fluoroscopy and the good soft tissue 3D anatomic information provided by MRI. However, to date, there has been no simple method to overlay MRI data onto fluoroscopy data. Current XMRF technology requires the use of external fiducial markers, specialized x-ray systems, or 3D rotational radiocontrast runs, which makes it impractical to perform XMRF on a routine clinical basis. We report on a new XMRF method that can now be done quickly with commercially available software, without the need for contrast, customized x-ray systems, or external fiducial markers. Furthermore, the method only uses minimal radiation, making it feasible to routinely perform XMRF during catheterization procedures. We have used this modality during congenital heart disease catheterization in 23 patients. We have found XMRF useful for roadmapping, angiographic camera angle selection, and for device positioning. This catheterization modality has the potential to significantly reduce radiation exposure and improve catheterization outcomes.

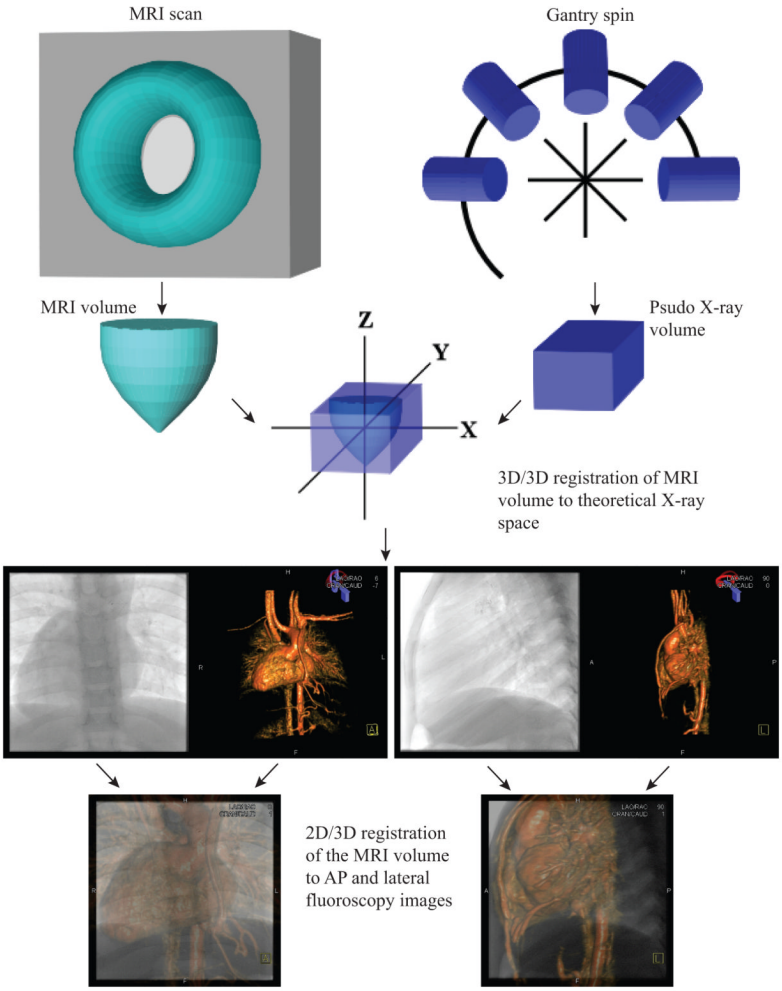

Figure 1.
XMRF registration protocol. Images at the bottom of the figure show the result of the registration process as seen with the AP camera in the AP (bottom left) projection and with the AP camera rotated to the lateral projection (bottom right).

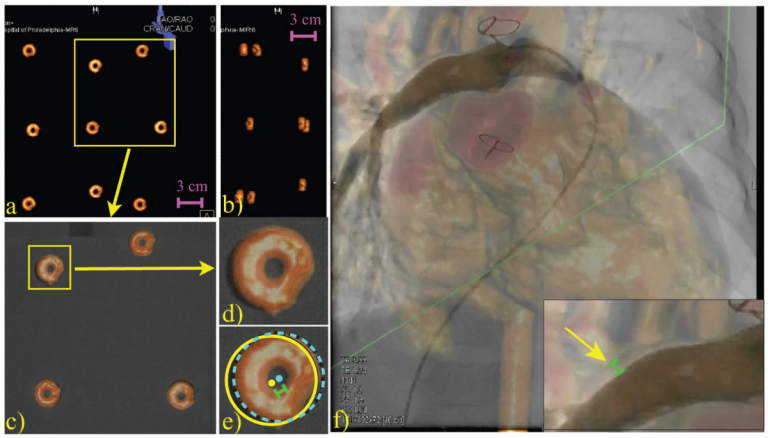

Figure 2.

Method used for error calculation. **A** and **B**, Volume-rendered MRI image of the phantom in the AP and lateral projections. **C**, AP projection of 4 dual-modality markers enclosed by the box in **A** fused to the x-ray image. **D**, Magnified view of overlaid marker is seen. **E**, The same marker is seen with a light blue dashed line surrounding the marker as seen on the MRI image and a yellow solid line surrounding the same marker as seen on the x-ray image. The error was calculated as the distance between the center of the 2 circular regions (light green bar). **F**, Contrast injection into the proximal right pulmonary artery (RPA) with insert showing a magnified view of the RPA. Yellow arrow points to the location where the error was measured; the green bar indicates the magnitude of the error at this location.

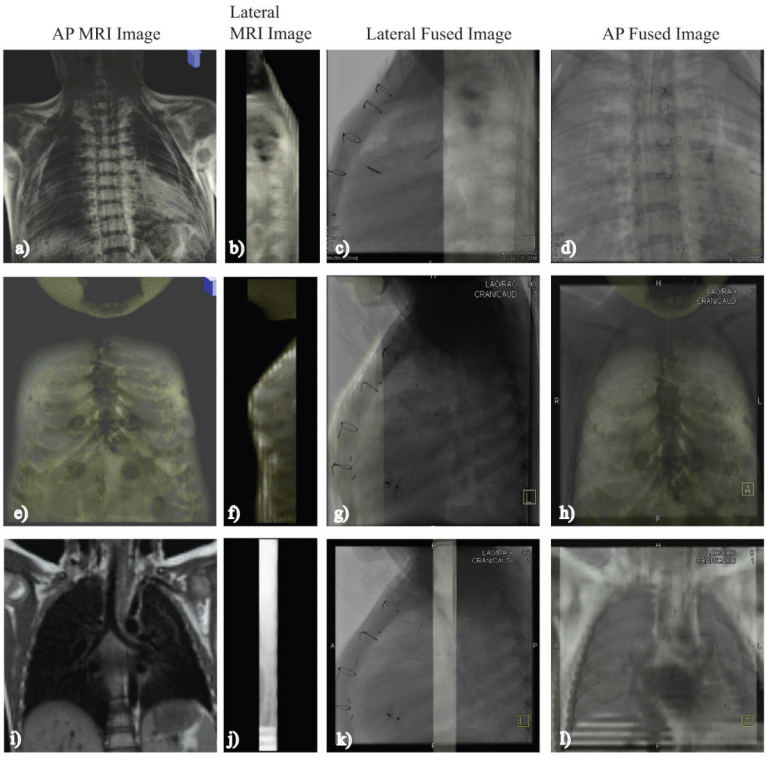

Figure 3.
Shows XMRF to the spinal cord (**A** through **D**), sternum (**E** through **H**), and the airway (**I** through **L**).

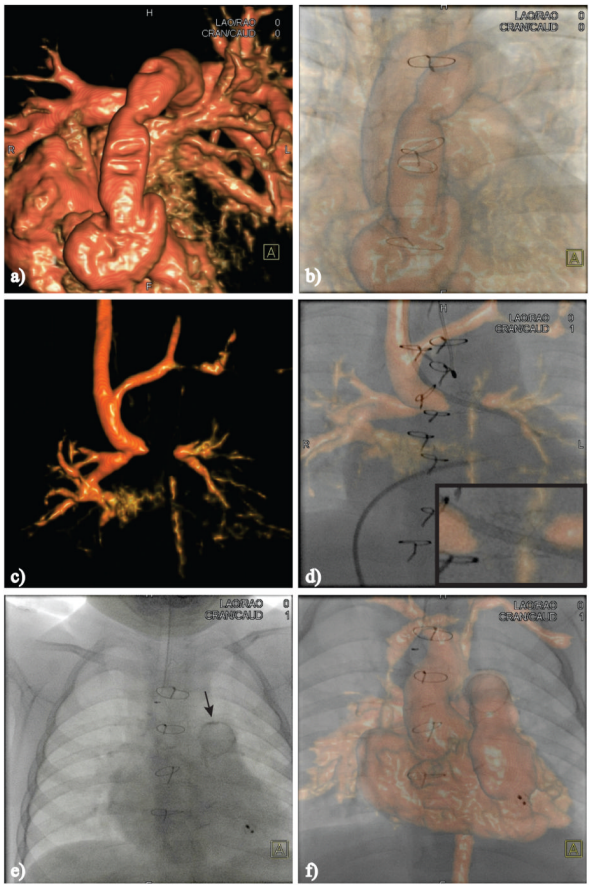

Figure 4.

A and **B**, XMRF to imaging artifact from sternal wires that resulted in indents on an RV-PA conduit. **C** and **D**, Susceptibility artifact from a stent produced a gap in the MRI image of the left pulmonary artery in a patient with a Glenn shunt. **D**, Insert shows a close-up view of the stent registered between the 2 PA stumps. **E** and **F**, Registration to distal conduit calcification. Arrow in **E** points toward a ring of calcification that formed at the distal end of a RV-PA conduit. All images are in the AP projection.

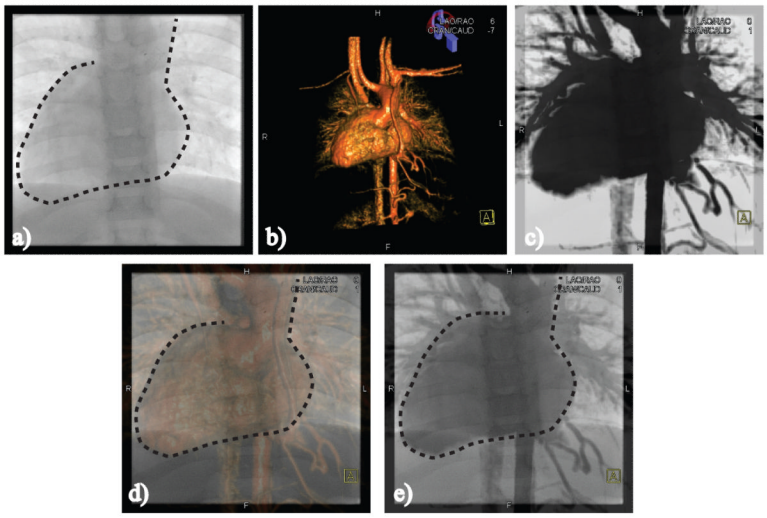

Figure 5.

A, Dashed line traces the heart border and the left lateral border of the aorta on the x-ray image. **B**, XMRF to heart and vessel borders using volume-rendered MRI image; **C,** maximal intensity projection–rendered image showing the largest cross-section of the heart and great vessels. **D** through **E**, Registered volume-rendered MRI and maximal intensity projection images. All images are in the AP projection.

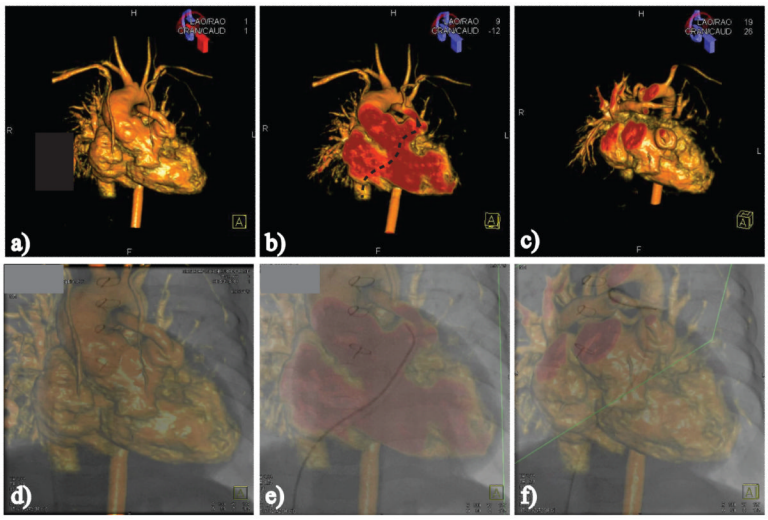

Figure 6.

A through **C**, Images of a patient with a small RV-PA conduit that were stored as a collection of bookmarks for roadmapping; **D** through **F**, the same images during the catheterization process. **B**, Pathway from the inferior vena cava to the entrance to the conduit is shown (dashed arrow) on an image that was created with an AP cut-plane. **E**, Corresponding catheter course is shown. **C,** Roadmap image that was created with an oblique cut-plane exposing the PA confluence and a hypoplastic left pulmonary artery (LPA). **F**, Corresponding catheter course with the tip of the catheter positioned in the distal LPA.

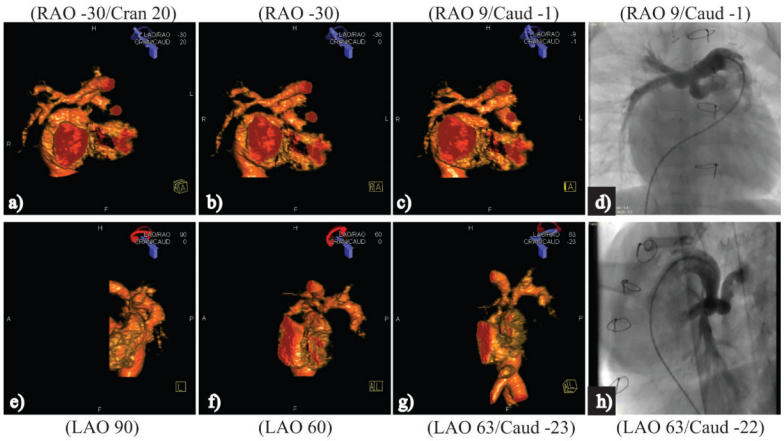

Figure 7.

Camera angle selection in a patient with complex PA anatomy. In this case, the left pulmonary artery (LPA) originated from the proximal right pulmonary artery and immediately took a 90° turn to the left. There was also proximal LPA hypoplasia. **A** through **D** correspond to the AP camera and **E** through **H** to the lateral camera. The anatomy is shown in the conventional camera angles (**A** and **B**, **E** and **F**) and in the angle that was chosen for the contrast angiogram (**C** and **G**). **D** and **H**, Corresponding contrast angiograms.

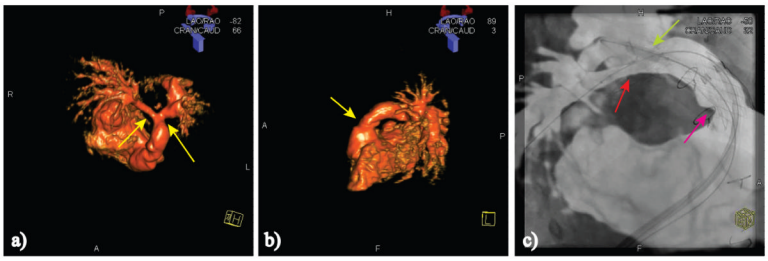

Figure 8.

Anatomy of a patient with an RV-PA conduit and bilateral proximal branch pulmonary artery stenosis (yellow arrows). **A** and **B**, Volume-rendered MRI images show the 3 stenotic regions. **C,** Image taken after a Palmaz XL 40×10-mm stent (Cordis) was placed using an 18×3.5 BiB (NuMed Inc) balloon in the proximal conduit (cyan arrow); a Genesis 3910B stent (Cordis) was placed with a 10×3.5 BiB in the proximal right pulmonary artery (RPA) (red arrow), and, simultaneously, a Genesis 2910B stent was placed using a 12×3 BiB in the proximal left pulmonary artery (light green arrow). **C,** Example of a nonperiodic error caused by distortion of the distal RPA by a stiff wire, resulting in the wire appearing to be outside of the vessel (light blue arrow).

Table 1

List of MRI Typical Imaging Parameters

	Bright Blood (SSFP)	Dark Blood (SE)	Cine (SSFP)	VEC	Twist
TR	120	800	30	30	2.5
TE	1.2	20	1.5	2.5	1
BW	1200	800	1200	400	800
ST, mm	3	3	4–6	4–5	1.5
Flip angle	90	180	90	25	25
Matrix	100×128	100×128	128×176	128×176	192×192
FOV	150×200	150×200	190×220	150×200	200×300

SSFP indicates steady-state free precession; SE, spin-echo; VEC, velocity-encoded phase contrast; BW, bandwidth; ST, slice thickness; and FOV, field of view.

Table 2

Summary of Patient Characteristics

Characteristic	(n=23)
Demographics	
Sex	Male, 14/23 (61%)
Age, y	3.59 (0.4–43.8)
Weight, kg	13.7 (3.6–90.1)
Height, cm	86 (25.2–169.4)
Anatomic category	
Glenn	7/23 (31%)
TGA	1/23 (4%)
Truncus	3/23 (13%)
Fontan	3/23 (13%)
TOF	8/23 (35%)
DILV	1/23 (4%)

TGA indicates transposition of the great arteries; TOF, tetralogy of Fallot; and DILV, double-inlet left ventricle.

Demographics data are reported as median with range and anatomic category data are reported as frequency with percentage of total count.

Table 3
Camera Angle Selection by Anatomic Type and Location

Patient	Diagnosis	Structure	AP Camera	Lateral Camera
1	Truncus	MPA, LPA	RAO 20/cran 13	LAO 63/caud 22
		RPA	RAO 9/caud 1	LAO 63/caud 22
2	Truncus	Conduit	RAO 37/cran 35	Lat 76/caud 6
		LPA	RAO 20/cran 35	LAO 76
		LPA	LAO 14	Lat 90
3	TOF	Conduit	RAO 9/cran 32	Lat 90
4	TOF	MPA	LAO 41/caud 2	LAO 118
		LPA	RAO 17/cran 49	LAO 84
		RPA	RAO 17/cran 18	LAO 65/caud 14
5	TOF	MPA	RAO 9/cran 52	LAO 80/caud 2
		LPA	LAO 23/cran 10	LAO 80/caud 2
6	TGA	LPA	LAO 32/cran 17	lat 90
7	TOF	RPA	RAO 23	LAO 63/caud 10
8	TOF	LPA	RAO 3	LAO 70
9	Truncus	LPA	LAO 20/cran 32	lat 90
10	TOF	RPA	RAO 26	LAO 53/caud 20
		LPA	RAO 43/caud 6	LAO 75
11	TOF	RPA	RAO 23/caud 12	LAO 68

TOF indicates tetralogy of Fallot; TGA, transposition of the great arteries; MPA, main pulmonary artery; LPA, left pulmonary artery; RPA, right pulmonary artery; cran, cranial angulation; caud, caudal angulation; and lat, lateral angulation.

Only structures that were imaged using the MRI data for camera angle selection are listed.